

## An Empirical Test and Calibration of H II Region Diagnostics

Robert C. Kennicutt, Jr.,<sup>1,2</sup> Fabio Bresolin,<sup>3,4</sup> Howard French,<sup>5,6</sup> Pierre Martin<sup>7</sup>

### ABSTRACT

We present spectrophotometry in the 3600–9700 Å region for a sample of 39 H II regions in the Galaxy and Magellanic Clouds, for which independent information is available on the spectral types and effective temperatures of the ionizing stars. The spectra have been used to evaluate nebular diagnostics of stellar temperature, metal abundance, and ionization parameter, and compare the observed behavior of the line indices with predictions of nebular photoionization models. We observe a strong degeneracy between forbidden-line sequences produced by changes in stellar  $T_{eff}$  and metal abundance, which severely complicates the application of many forbidden-line diagnostics to extragalactic H II regions. Our data confirm however that the Edmunds & Pagel [O II]+[O III] abundance index and the Vílchez & Pagel  $\eta'$  index provide more robust diagnostics of metal abundance and stellar effective temperature, respectively. A comparison of the fractional helium ionization of the H II regions with stellar temperature confirms the reliability of the spectral type vs  $T_{eff}$  calibration for the relevant temperature range  $T_{eff} \leq 38000$  K. We use empirical relations between the nebular hardness indices and  $T_{eff}$  to reinvestigate the case for systematic variations in the stellar effective temperatures and the upper IMFs of massive stars in extragalactic H II regions. The data are consistent with a significant softening of the ionizing spectra (consistent with cooler stellar temperatures) with increasing metal abundance, especially for  $Z \leq Z_{\odot}$ . However unresolved degeneracies between  $Z$  and  $T_{eff}$  still complicate the interpretation of this result.

*Subject headings:* galaxies: ISM — galaxies: star clusters — H II regions

---

<sup>1</sup>Steward Observatory, University of Arizona, Tucson, AZ 85721

<sup>2</sup>Visiting Astronomer, Cerro Tololo Interamerican Observatory, National Optical Astronomical Observatories, which are operated by AURA, Inc., under contract with the National Science Foundation.

<sup>3</sup>European Southern Observatory, Karl-Schwarzschild-Str. 2, D-85748 Garching b. München, Germany

<sup>4</sup>Present address: Institut für Physik und Astronomie, Scheinerstr. 1, D-81679, Munich, Germany

<sup>5</sup>Department of Astronomy, University of Minnesota, 116 Church Street SE, Minneapolis, MN 55455

<sup>6</sup>Honeywell Technology Center, 3660 Technology Drive, Minneapolis, MN 55418

<sup>7</sup>CFHT, P.O. Box 1597, Kamuela, HI 96743

## 1. INTRODUCTION

Over the past 15 years high-quality emission-line spectra have been obtained for hundreds of H II regions in nearby spiral and irregular galaxies. The primary use of these data has been to study the chemical composition patterns in galactic disks (e.g., McCall, Rybski, & Shields 1985, Vila-Costas & Edmunds 1992, Zaritsky, Kennicutt, & Huchra 1994, Dinerstein 1996). However with the availability of state-of-the-art photoionization codes such as CLOUDY (Ferland et al. 1998), combined with stellar population synthesis codes for young clusters (e.g., Leitherer & Heckman 1995, Leitherer et al. 1999), H II region spectra are being applied increasingly to measure the ages and initial mass functions (IMFs) of the ionizing star clusters (e.g., Vílchez & Pagel 1988, Shields 1990, Stasińska & Leitherer 1996, Bresolin, Kennicutt, & Garnett 1999, hereafter BKG). Similar techniques have been applied to model the infrared emission-line spectra of IR-luminous starbursts, and the results have been interpreted as evidence for an anomalous IMF in these objects (e.g., Rieke et al. 1993).

A basic limitation in this approach is its reliance on a long chain of theoretical inputs: stellar evolution models as functions of stellar mass, chemical composition and mass-loss rates; stellar atmosphere models as functions of effective temperature, surface gravity, chemical composition, and mass-loss properties, and photoionization models for the surrounding H II region. The derived nebular abundances tend to be insensitive to the details of these models, but the inferred properties of the ionizing stars are sensitive to the model inputs at every step in the chain. The problem is especially acute when using H II region or starburst spectra to constrain the effective temperatures and IMFs of the ionizing stars (e.g., Mathis 1985, McCall et al. 1985, Vílchez & Pagel 1988, BKG). Most studies show evidence for a systematic softening of the ionizing continuum of H II regions with increasing metal abundance, but the absolute range in stellar effective temperatures is highly model dependent, and the case for a systematic variation in the upper IMF is shaky at best (BKG and references therein).

Another approach, which can circumvent many of these difficulties, is to test the nebular diagnostics empirically, by obtaining spectra for nearby H II regions which are ionized by stars of known spectral type. This makes it possible to anchor the nebular indicators of stellar temperature directly to the stellar spectral classification system. Furthermore, by modeling these H II regions with the same methods that are applied to extragalactic regions one can directly assess the reliability of the model-based approach.

This empirical approach was first explored by Chopinet & Lortet-Zuckermann (1976) and Kaler (1978) to calibrate the  $[\text{O III}]\lambda 5007/\text{H}\beta$  ratio as an indicator of stellar effective temperature. For studies of extragalactic H II regions and starbursts a more robust hardness index than  $[\text{O III}]/\text{H}\beta$  is desirable, because the excitation of  $[\text{O III}]$  varies locally within H II regions, and it is sensitive to other physical parameters (e.g., metal abundance, ionization parameter, dust) which can vary systematically in galaxies (e.g., Kennicutt 1984, Shields 1990). Other hardness indices have been developed for extragalactic applications (e.g., Vílchez & Pagel 1988), but their reliability has not

been tested empirically.

In this paper we report the results of a spectrophotometric study of 39 H II regions in the Galaxy, the LMC, and the SMC, which is aimed at providing an empirical foundation for nebular-based measurements of the stellar ionizing continuum and IMF in galaxies. We use the spectra to evaluate several nebular diagnostics of massive stellar populations, and to compare the known properties of the stars in these regions with those inferred from photoionization modeling. Our study is mainly motivated by applications to stellar temperatures and IMFs, but the approach is more generally applicable to spectral modeling of extragalactic H II regions and starbursts. This paper is complementary in approach to a recent analysis of Oey et al. (2000), which has addressed many of these same questions using detailed point-by-point observations of 4 H II regions in the LMC.

The remainder of this paper is organized as follows. The H II region sample and the observations are described in § 2 and § 3, respectively. In § 4 we analyze the behavior of the principal diagnostic line ratios and investigate several commonly applied abundance and spectral hardness indicators. In § 5 we apply the empirical calibration to constrain the range of stellar effective temperature and upper IMF in galactic disks.

## 2. H II REGION SAMPLE AND PROPERTIES

Since the first prerequisite for this work is knowledge of the exciting stars in the calibrating H II regions, the ideal approach is to observe small Galactic H II regions ionized by single stars (or a few stars) of known spectral type. Such “calibrating” objects comprise approximately half of our sample, while the remaining objects, ionized by larger OB associations or clusters, provide the link to the brighter class of H II regions observed in external galaxies.

The calibrating H II regions were selected to span the maximum available range in stellar spectral type and effective temperature. Preference was given to nebulae with angular diameters that fit within the length of the spectrograph slit ( $3' - 6'$ ), and to regions with low to moderate extinction, with  $E(B - V) < 2$  mag in most cases. Most of our sample was drawn from the northern survey of small Galactic H II regions defined by Hunter & Massey (1990; =HM90), and the southern sample of H II regions studied by Shaver et al. (1983) in their abundance survey of the Milky Way. Identifications and spectral types for the ionizing stars were taken directly from HM90 for the northern sample, and from a variety of published sources for the southern objects. Most of the latter derive from classification work in the 1970’s by Georgelin and collaborators (e.g., Georgelin, Georgelin, & Roux 1973, Chopinet, Georgelin, & Lortet-Zuckermann 1973). Table 1 lists the main properties of the H II regions in our sample, including the sources of the stellar spectral types and oxygen abundances. Column 8 indicates the observatory used to obtain the spectra, and asterisks denote objects in the calibrating subsample.

It is relatively easy to compile an adequate sample of small H II regions ionized by single stars

of type O6V and later ( $T_{eff} \leq 42000$ ). However this becomes nearly impossible for hotter O stars, because such stars almost always form in rich OB associations along with numerous later-type stars. The contribution of the cooler stars to the ionizing continuum can be significant, and this composite ionization needs to be taken into account in the determination of  $T_{eff}$ . We observed several of these large Galactic H II regions, including M8, M16, M17, the Rosette nebula (S275), the Carina nebula, and the giant H II region NGC 3603. We used the most recent studies of their stellar contents, including near-infrared observations in many cases, to identify all of the principal ionizing stars. In order to extend our coverage to even higher stellar temperatures, we also observed four H II regions ionized by early-type Wolf-Rayet stars, the Galactic regions RCW 5 = NGC 2359 (WN4), RCW 48 = NGC 3199 (WN5), and the LMC regions DEM 174 (WN4p) and DEM 231 (WN3).

The remainder of our sample consists of much larger H II regions located in the LMC and SMC. Most of these objects are physically distinct from the smaller Galactic H II regions, being ionized by much more populous OB associations, and as such are less suitable for our empirical calibration of nebular diagnostics. However these objects are directly analogous to the more distant extragalactic H II regions, and their stellar contents have been cataloged by various authors (Table 1), so we can analyze them on the same basis as the smaller Galactic H II regions.

To assign a stellar effective temperature to the H II regions we have adopted the spectral type– $T_{eff}$  calibration by Vacca, Garmany and Shull (1996), together with the stellar ionizing fluxes predicted by Schaerer & de Koter (1997). The resulting temperatures and luminosities are listed in columns 4 and 5 of Table 1. In the case of an ensemble of hot stars, a mean temperature was derived by summing the  $\text{He}^0$  and  $\text{H}^0$  ionizing fluxes of all of the stars, and calculating the effective temperature of a class V star having the same  $Q_1/Q_0$  ratio ( $\text{He}^0$  to  $\text{H}^0$  total ionizing flux ratio). Effective temperatures for the W-R stars were estimated using the semi-empirical calibration of Esteban et al. (1993). More detailed information on the stellar contents of the individual H II regions is given in the Appendix.

Oxygen abundances, expressed as  $12+\log(\text{O}/\text{H})$ , are given in column 6, and their sources are indicated in column 7. When abundances were unavailable in the literature and could not be measured directly from our spectra, we estimated the abundance using the empirical indicator  $R_{23} = ([\text{O III}]\lambda\lambda 4959, 5007 + [\text{O II}]\lambda\lambda 3726, 3729) / \text{H}\beta$  (Pagel et al. 1979), as calibrated by Edmunds and Pagel (1984). These estimates are listed in parentheses in Table 1. The accuracy of the  $R_{23}$ -based abundances is of order  $\pm 0.2$  dex, but this is sufficient for our purposes.

Figure 1 shows the range of stellar temperatures and oxygen abundances for the H II regions in our sample. Squares and round points denote calibrating and non-calibrating H II regions with direct (electron temperature based) abundance measurements, respectively. Open triangles indicate those regions with empirical ( $R_{23}$ ) abundance estimates. The H II regions cover a stellar temperature range of 32000 – 48000 K, with the Wolf-Rayet nebulae extending to 67000 K. The 28 Galactic H II regions span a range of O/H abundances of  $-0.5 \leq [\text{O}/\text{H}] \leq 0.0$  (assuming  $12+\log(\text{O}/\text{H})_{\odot} =$

8.9), while the 9 LMC regions cluster around  $[O/H] \simeq -0.4$ , and the single SMC region (N66 = NGC 346) has  $[O/H] = -0.7$ .

The range of abundances in the sample is important for the interpretation which follows, because changes in metal abundance can mimic many of the trends in nebular spectra that are produced by changes in stellar temperature or IMF. For lack of a better prescription we have adopted a single conversion of spectral type to  $T_{eff}$  in our analysis, independent of abundance, and this conceivably could introduce some coupling between the two parameters (§ 4.3). Fortunately, Fig. 1 shows that  $Z/Z_{\odot}$  and  $T_{eff}$  are largely decoupled from each other in our sample, and this should allow us to separate their effects on the nebular spectra.

### 3. OBSERVATIONS AND DATA REDUCTION

Our data consist of spectrophotometry covering the wavelength range 3600–9700 Å. The extended coverage to the near-infrared includes the [S III]  $\lambda\lambda 9069, 9532$  doublet, which when combined with measurements of [S II]  $\lambda\lambda 6716, 6731$ , [O II]  $\lambda 3727$ , and [O III]  $\lambda\lambda 4959, 5007$  provides a robust measure of the hardness of the ionizing stellar continuum (Mathis 1985, Vílchez & Pagel 1988).

#### 3.1. Steward Observatory Data

Spectra of the northern sample of Galactic H II regions were obtained in 1993 Oct and 1995 Jun with the B&C CCD spectrograph on the Bok telescope, equipped with a thinned Loral  $800 \times 1200$  element CCD detector. Two grating settings were used to cover the full spectral range. A  $400 \text{ g mm}^{-1}$  grating blazed at 4800 Å provided coverage of the 3600–6900 Å region, hereafter denoted as the “blue” spectra. A second set of “red” spectra were obtained with a  $400 \text{ g mm}^{-1}$  grating blazed at 7500 Å to cover the 6400–9700 Å region. A slit width of  $2''.5$  provided a spectral resolution of 8 Å FWHM. The full spatial coverage of a spectrum was  $3''.5$ , with a single pixel on the detector projecting to  $0''.83$  on the sky. Spectra of NGC 7538 and NGC 7635 were obtained in 1988 Nov using the same spectrograph but with a  $800 \times 800$  element Texas Instruments CCD detector. The same setup was used for the red spectra, but the blue spectra were obtained with a  $600 \text{ g mm}^{-1}$  grating blazed at 3570 Å, to cover the region between 3700–5100 Å.

Figure 2 shows images of the H II regions, with the slit positions superimposed. Most of the images were taken from the Digitized Sky Surveys<sup>8</sup>. The H II regions were observed at a fixed position extending E–W through the center of the nebula (but offset from bright stars to avoid contamination of the spectrum), and also in a drift scanned mode, where the image of the H II region was trailed across the slit to provide an integrated spectrum. Comparison of the fixed and scanned spectra (integrated over the length of the slit in both instances) reveals surprisingly small differences in the main diagnostic line ratios, indicating that the fixed pointings provide a representative sampling of the nebula. This is illustrated in Figure 3, which compares the behavior

of  $[\text{O III}]/\text{H}\beta$  vs  $[\text{N II}]/\text{H}\alpha$  and  $[\text{S II}]/\text{H}\alpha$  for the two sets of spectra, with each pair of observations connected. Most of the differences follow the trajectories expected from changes in the nebular ionization parameter. We have chosen to analyze the fixed position data, in order to take advantage of their higher signal/noise, and to maintain consistency with the CTIO data, which were taken as fixed pointings. The only exception is the very large H II region M8 (S25), which shows a large inconsistency between fixed and scanned spectra, presumably because the former is strongly influenced by local variations in ionization structure. In that case we use the drift scanned spectrum, which samples a region of  $10' \times 3'$  (EW  $\times$  NS), centered on the position listed in Table 1 (see Fig. 2d).

Exposure times of 300–1200 sec were chosen to provide accurate spectrophotometry of the bright diagnostic lines ( $\text{S/N} > 20$  in most cases). The fainter auroral lines such as  $[\text{O III}] \lambda 4363$  were not a target of this study, and in many cases they were too weak in our spectra to be useful. The spectrophotometric flux calibration was determined using standard stars from Massey et al. (1988) for the blue spectra, and stars from Oke & Gunn (1983) for the red spectra. The observations were made with  $2''.5$  and  $4''.5$  wide slits, oriented to limit errors from atmospheric dispersion effects to  $< 0.05$  mag across the wavelength range.

### 3.2. CTIO Data

The southern Galactic H II regions and all of the LMC and SMC H II regions were observed in 1987 Jan, 1987 Dec, and 1988 Jan using the CTIO 1.0 m and 1.5 m telescopes. At the time that these observations were made a blue-sensitive CCD detector was not available, so the blue spectra were obtained with a 2D FRUTTI photon counting detector system on the 1.0 m Cassegrain spectrograph. The instrument was configured with a  $600 \text{ g mm}^{-1}$  grating blazed at  $5000 \text{ \AA}$  and WG-360 blocking filter, which provided coverage of  $3600\text{--}7000 \text{ \AA}$  and a resolution of  $6 \text{ \AA}$  FWHM when used with an  $8'' \times 6'$  slit. All observations were made with the slit oriented E–W at a fixed position, usually centered  $10''$  south of the central star. Due to the limited dynamic range of the 2D FRUTTI detector, observations of bright regions were made with neutral density filters, and exposure times for most objects were 900–1800 sec, largely independent of surface brightness. Standard stars from Stone & Baldwin (1983) were observed with a  $12''$  wide slit for flux calibration.

Red spectra were obtained with the Cassegrain spectrograph on the CTIO 1.5 m telescope, equipped with an unthinned  $385 \times 576$  GEC CCD detector. Two grating settings were used for most of the objects. A  $158 \text{ g mm}^{-1}$  grating blazed at  $8000 \text{ \AA}$  in first order and a OG-550 blocking filter provided complete coverage of the  $5730\text{--}10200 \text{ \AA}$  region, with a resolution of approximately  $20 \text{ \AA}$

---

<sup>8</sup>The Digitized Sky Surveys were produced at the Space Telescope Science Institute under U.S. Government grant NAG W-2166. The images of these surveys were based on photographic data obtained using the Oschin Schmidt Telescope at Palomar Mountain and the UK Schmidt Telescope. The plates were processed into the present digital form with the permission of these institutions.

FWHM when used with a  $6'' \times 6'$  slit. A second set of spectra were obtained using a  $600 \text{ g mm}^{-1}$  grating blazed at  $6750 \text{ \AA}$ , to cover the region  $5650\text{--}6850 \text{ \AA}$  at  $5 \text{ \AA}$  resolution, again with a  $6''$  slit. The low-resolution spectra were used primarily to measure the diagnostic lines longward of  $7000 \text{ \AA}$  (mainly [S III]  $\lambda\lambda 9069, 9532$  and [Ar III]  $\lambda 7135$ ), while the higher-resolution spectra provided the best measurements of the [N II]  $\lambda\lambda 6548, 6583$ , [S II]  $\lambda\lambda 6716, 6731$ , and He I  $\lambda 6678$  lines. Exposure times ranged from 120 to 1800 sec. Standard stars from Stone and Baldwin (1983) and Baldwin & Stone (1984) were observed with a  $12''$  slit.

In order to investigate the local variation in the nebular diagnostic indices within individual H II regions, we obtained spectra at additional positions in the Carina and 30 Doradus H II regions, as shown in Figures 2c and 2g, respectively. The observations of 30 Dor include a series of five positions extending E–W a total of  $24'$  through the center of the H II region. We also obtained red spectra only at 22 other positions in 30 Dor and 12 positions in the Orion nebula, to match previous observations at  $3700\text{--}7200 \text{ \AA}$  by Mathis, Chu, & Peterson (1985) and Peimbert & Torres-Peimbert (1977), respectively. Charts showing the positions of these measurements can be found in the original papers. The red spectra were used to extend the wavelength coverage of the published measurements to the [S III]  $\lambda\lambda 9069, 9532$  lines. We used the overlapping coverage of the  $H\alpha$ , [N II], and [S II] lines to firmly tie in the [S III] fluxes, and confirm that the identical regions were observed.

### 3.3. Data Reduction and Calibration

The spectra were reduced using the two-dimensional spectrum reduction package in IRAF<sup>9</sup>, following conventional procedures. We limit the discussion here to reductions and tests that were unique to this data set. Spatial distortions in the long-slit spectra were removed using comparison lamp exposures. The distortions were considerable in the 2D FRUTTI data, and data within 5–10% of the slit edges were excluded in subsequent reductions. The 2D FRUTTI spectra were checked for deadtime effects in the bright lines, using short exposures obtained with darker neutral filters, and by comparing the observed [O III]  $\lambda\lambda 4959, 5007$  doublet ratio (the strongest feature in most raw spectra) to its theoretical value. Deadtime effects were present in only a small fraction of the spectra, and in such cases the [O III]  $\lambda 5007$  line was discarded, and the scaled flux of [O III]  $\lambda 4959$  was used instead. Similar checks were carried out with multiple neutral density filters on the standard stars, and measurements with any hint of a saturation problem were discarded.

Calibration of the red CCD spectra in the [S III]  $\lambda\lambda 9069, 9532$  region also required special care, due to the presence of unresolved telluric water absorption lines. To maximize the reliability of the [S III] measurements we made frequent observations of subdwarf standard stars located at the same airmass as the H II regions, and used a high-order spline fit to the stellar spectra to

---

<sup>9</sup>IRAF is distributed by the National Optical Astronomical Observatories, which are operated by AURA Inc., under contract with the National Science Foundation.

remove the absorption on wavelength scales of  $>50 \text{ \AA}$  (exclusive of the regions around the Paschen emission lines, which are influenced by absorption lines in the standard stars). The reliability of this procedure was confirmed by the degree of consistency of the observed [S III]  $\lambda\lambda 9069, 9532$  doublet ratios with its theoretical value (2.44), and by the shapes of the calibrated continuum spectra in the H II regions themselves. As a conservative measure we attach a mean uncertainty of  $\pm 20\%$  to the summed [S III]  $\lambda\lambda 9069, 9532$  fluxes.

The overall precision of the spectrophotometry was determined from comparisons of multiple observations of the same objects, intercomparison of the blue and red spectra in the overlapping wavelength regions, and from the measured ratios of the [O III] and [S III] doublets. The typical uncertainties for strong lines range from  $\pm 5\%$  or better for the Bok CCD spectrophotometry (excluding the [S III] lines) to  $\pm 10\%$  for the CTIO blue spectra (2D FRUTTI) and  $\pm 20\%$  for the [S III] fluxes and the CTIO [O II] fluxes. External comparisons with published sources such as Dufour (1975), Shaver et al. (1983), Mathis et al. (1985), and Hunter (1992) show consistency to the degree that is expected given the measuring errors above and differences in positions and aperture sizes. The only exception is a tendency for the He I  $\lambda 5876$  fluxes measured at CTIO (2D FRUTTI) to be significantly lower than those from published sources, and consequently we attach more weight to the He I  $\lambda 6678$  (CCD) data in these objects.

### 3.4. Emission-Line Measurements

A one-dimensional spectrum of each region was extracted by summing over the radial extent of the H II region on the slit. Whenever possible a background sky measured from the outer parts of the slit was subtracted, but when the H II region filled the slit the sky was included and subtracted in the fitting of each line flux (after confirming the absence of sky line contamination). Analysis of the extracted 1D spectra followed standard procedures. Line fluxes were measured by a direct integration of the line profile, with subtraction of a linearly interpolated continuum, using either the SPLOT task in IRAF or our own software. The flux scales of the blue and red spectra were tied together using the sum of the  $H\alpha$  and [N II]  $\lambda\lambda 6548, 6583$  lines.

Reddening corrections were derived from the Balmer decrement ( $H\alpha, H\beta, H\gamma$ ), the theoretical Balmer line ratios as calculated by Hummer & Storey (1987), and the average interstellar reddening curve from Cardelli, Clayton, & Mathis (1989). When measured electron temperatures and densities were available, either from the literature or from our spectra, they were used to determine the theoretical Balmer decrement; otherwise a temperature of 10000 K and density of  $100 \text{ cm}^{-3}$  were assumed.

Table 2 lists the reddening-corrected line fluxes for the principal diagnostic lines, as well as the logarithmic extinction at  $H\beta$  (column 2). All fluxes are normalized to  $f(H\beta) = 100$ . For H II regions with multiple measurements we have listed the fluxes for a single representative position. Complete line lists, including the fainter lines and the multiple position measurements are available



from the authors upon request.

## 4. ANALYSIS

Before we specifically address the nebular diagnostics of abundance and stellar temperature, it is instructive to examine the behavior of the H II region spectra using the well-known diagnostic diagrams of Baldwin, Phillips, & Terlevich (1981), and compare them to the spectra of more distant and luminous extragalactic H II regions.

To aid in the physical interpretation of these diagnostic diagrams, we have computed a set of CLOUDY nebular models (Ferland et al. 1998), using non-LTE stellar atmosphere models by the Munich group (Pauldrach et al. 1998) as the source of ionizing photons, as described in BKG. These will be used later to compare the stellar effective temperatures from nebular model fitting to the actual effective temperatures of the exciting stars. However in this section the main use of the models will be to illustrate how changes in metal abundance, stellar temperature, or ionization parameter affect the various line ratios.

### 4.1. Diagnostic Diagrams and Ionization Parameter

Figure 4 shows two of the most commonly used diagnostic diagrams for extragalactic H II regions and AGNs, with the excitation ratio  $[\text{O III}]\lambda 5007/\text{H}\beta$  plotted against  $[\text{N II}]\lambda 6583/\text{H}\alpha$  and  $[\text{S II}]\lambda\lambda 6716, 6731/\text{H}\alpha$ . Here and in the following figures we have subdivided the sample: solid squares mark the calibrating Galactic H II regions ionized by one (or a few) OB stars; open squares correspond to the more luminous Galactic H II regions ionized by associations of OB stars with a range of spectral types; open circles denote the LMC and SMC regions, and open stars indicate the four nebular ionized by early-type W-R stars. For comparison we have plotted with small triangles the same line ratios for a large sample of extragalactic H II regions in Sa–Im galaxies, from BKG.

Extragalactic H II regions show a tight spectral sequence in both of these diagrams (McCall, Rybski, & Shields 1985, Kennicutt & Garnett 1996), which often is interpreted as evidence that giant H II regions are predominantly radiation bounded objects (McCall et al. 1985). Figure 4 shows that the much smaller Galactic H II regions also lie on this same sequence. The correspondence is especially tight in the case of  $[\text{O III}]/\text{H}\beta$  vs  $[\text{N II}]/\text{H}\alpha$ , where the sequences are virtually indistinguishable. The WR nebulae lie well above the sequence, which reflects the very high effective temperatures of these stars ( $T_{\text{eff}} \geq 55000$  K). The LMC H II regions show a slight tendency toward weaker  $[\text{N II}]$  emission, which probably reflects the anomalous N/O ratio in this galaxy (Garnett 1999).

In extragalactic H II regions the tight spectral sequences (Fig. 4) are mainly interpreted as being abundance sequences (e.g., Searle 1971, Shields & Searle 1978, Pagel & Edmunds 1978, Mc-

Call et al. 1985). However in our sample the primary variable along the sequence is not abundance but stellar temperature. This is shown in Figure 5, which again shows the [O III]/H $\beta$  vs [N II]/H $\alpha$  relation, but this time with the points coded by stellar temperature (left) and by oxygen abundance (right). Although both parameters clearly influence the position of H II regions along the sequence, variations in  $T_{eff}$  clearly dominate in this sample. The virtual indistinguishability between this  $T_{eff}$  sequence with the extragalactic “abundance” sequence illustrates the degeneracy between temperature and abundance (and to some degree ionization parameter) in this type of diagnostic diagram. In hindsight this may help to explain why it has proven so difficult to disentangle variations in ionization temperature and IMF from abundance variations in extragalactic H II regions.

The correspondence between the Galactic and extragalactic sequences is much poorer for [O III]/H $\beta$  vs [S II]/H $\alpha$ , with the small Galactic H II regions showing systematically weaker [S II] emission (Fig. 4). A comparison with the driftscanned spectra in Fig. 3 shows that this is partly due to the spatial undersampling of our slit spectra, but the remainder of the difference appears to be a systematic difference in mean ionization parameter between the two samples. This is quantified in Figure 6, which plots the ionization-sensitive ratio [S II]  $\lambda\lambda 6716, 6731$ /[S III]  $\lambda\lambda 9069, 9532$  as a function of  $T_{eff}$  of the ionizing stars (same symbols as Fig. 4). The [S II]/[S III] ratio is commonly used as a diagnostic of the nebular ionization parameter  $U$  (Díaz et al. 1991), defined in this case as the ratio of ionizing photon to electron densities. It can be expressed as:

$$U = \frac{Q_{H^0}}{4\pi R_S^2 n c} \quad (1)$$

where  $Q_{H^0}$  is the ionizing luminosity of the stars (photons per sec),  $R_S$  is the Strömgen radius of the H II region,  $n$  is the electron density, and  $c$  is the speed of light. Superimposed on Fig. 6 are photoionization models for values of  $\log U$  between  $-1.5$  and  $-4.0$  (see BKG for details). Most of the regions studied here lie in the range of  $-3.5 \leq \log U \leq -1.5$ , whereas most bright extragalactic H II regions lie in a narrower range with  $-3.5 \leq \log U \leq -2.5$  (BKG). The difference primarily reflects the larger aperture sizes in extragalactic studies (typically hundreds of parsecs in projected diameter). This difference is not large enough to affect the comparison of  $U$ -insensitive indices such as the abundance parameter  $R_{23}$  and the nebular hardness parameter  $\eta'$  (§4.3), but it may need to be taken into account when applying more ionization-sensitive indices such as [O III]/H $\beta$ , [Ne III]/H $\beta$ , or [O III]/[N II] (below).

## 4.2. Abundance Indices

The backbone of the extragalactic abundance scale rests on direct electron temperature based measurements, but in metal-rich H II regions the temperature-sensitive auroral lines are unobservable, and most abundance information in that regime is based on “empirical” excitation indices such as  $R_{23}$  (Pagel et al. 1979) or [O III] $\lambda 5007$ /[N II] $\lambda 6583$  (Alloin et al. 1979). Our data are not of sufficient quality to improve on the existing calibrations of these indices, but we can use our spatially resolved observations of 30 Dor, Carina, and Orion to investigate the robustness of the

empirical abundance indices. Do spectra of different regions in the same object yield consistent abundances?

As a test of the  $R_{23}$  index, the left panel of Figure 7 shows the relation between  $[\text{O III}] \lambda\lambda 4959, 5007/\text{H}\beta$  and  $[\text{O II}] \lambda 3727/\text{H}\beta$  (with linear scales) for the multiple positions in 30 Dor (open stars), Carina (triangles), and Orion (open circles). The 30 Dor data include spectra from Mathis et al. (1985) and the Orion data are all from Peimbert & Torres-Peimbert (1977). All three H II regions show a very large range of excitation across the regions sampled, with both  $[\text{O III}]/\text{H}\beta$  and  $[\text{O II}]/\text{H}\beta$  varying by factors of 2–5. However the sum of the line fluxes ( $R_{23}$ ) is relatively constant, as shown by the diagonal lines in Fig. 7. The constancy of  $R_{23}$  is especially impressive in 30 Doradus and Carina, where the dispersion in  $R_{23}$  transforms to a full range of  $<0.1$  dex in  $O/H$ . The  $R_{23}$  index is less well-behaved in Orion, though the range in abundances about the mean value is no larger than the calibration uncertainty of the method. Our results confirm a similar test applied to the giant H II region NGC 604 in M33 (Diaz et al. 1987), and suggest that even spatially undersampled observations of local H II regions may be useful for calibrating  $R_{23}$ .

Vílchez & Esteban (1996) and Díaz & Pérez-Montero (1999) have explored the use of the sum of the  $[\text{S II}]$  and  $[\text{S III}]$  forbidden-line strengths,  $S_{23} \equiv ([\text{S II}] \lambda\lambda 6716, 6731 + [\text{S III}] \lambda\lambda 9069, 9532)/\text{H}\beta$  as an empirical abundance index, in analogy to  $R_{23}$ . The main advantage of this index over  $R_{23}$  is its monotonic behavior as a function of oxygen abundance, and its insensitivity to the global degree of ionization of the nebula, at least for giant extragalactic H II regions. The right panel of Fig. 7 shows the behavior of this index for the multiple position observations of 30 Dor, Carina, and Orion. In contrast to  $R_{23}$  (left panel), the  $S_{23}$  values show much more scatter and nearly complete overlap between the three H II regions. This probably is due to a combination of observational error in the  $[\text{S III}] \lambda\lambda 9069, 9532$  measurements and large local variations in  $[\text{S II}] \lambda\lambda 6716, 6731/\text{H}\beta$ , which forms preferentially at the ionization interfaces and in shocks. The  $S_{23}$  ratio (and hence the inferred metal abundance) also varies systematically across the nebulae, especially in 30 Dor, where the data span the full range of radius in the H II region. This suggests that  $S_{23}$  should only be applied to global spectra of H II regions, which sample a representative fraction of the  $\text{S}^{++}$  and  $\text{S}^+$  emitting volumes. Despite the considerable scatter in  $S_{23}$  within each H II region, the corresponding dispersion in inferred metal abundances is only slightly larger than for  $R_{23}$ , due to the relatively weak  $Z$ -dependence of  $S_{23}$  in this excitation range, if the calibration of Díaz & Pérez-Montero (1999) is used.

Figure 8 shows a similar test of the  $[\text{O III}]/[\text{N II}]$  empirical abundance parameter. We would expect this ionization-sensitive index to show a larger dispersion within individual H II regions, and this is borne out in Fig. 8. The index shows a dispersion of  $\geq 1$  dex in all three H II regions, and the inferred abundance values overlap between the objects. The horizontal lines indicate the corresponding oxygen abundances in terms of  $12 + \log O/H$ , using the calibration of Dutil & Roy (1999); the inferred abundances show dispersions of  $\pm 0.2 - 0.3$  dex in a given H II region, about 2–3 times larger than for  $R_{23}$ . The relevance of these results for extragalactic applications is unclear, however. Comparisons of oxygen abundances derived from  $[\text{O III}]/[\text{N II}]$  and  $R_{23}$  have tended to

show excellent agreement across a wide range of excitation (Ryder 1995, Roy & Walsh 1997), and indeed the former abundances show a lower scatter, which suggests that the [O III]/N II] method can be reliable for luminous H II regions where the spectrophotometric aperture encloses most of the emitting volume. However it is also possible that the apparent consistency of the [O III]/N II] abundances is the result of a relatively narrow range of ionization parameters and other nebular properties within the samples that have been studied to date, and that this consistency could break down when applied to samples of H II regions with systematically different aperture sampling, ionization structure, or other nebular properties.

### 4.3. Diagnostics of Stellar Temperature and IMF

Emission-line spectra of H II regions and starbursts are being applied increasingly to constrain the ages and IMFs in the exciting star clusters (e.g., Stasińska & Leitherer 1996, Garcia-Vargas et al. 1997, BKG, Garnett 2000, and references therein). These applications rely on the ability to use nebular ionization models to characterize the shape and hardness of the ionizing continuum shortward of the Lyman break. In this section we use the sample of calibrating H II regions to directly assess several hardness parameters, ranging from robust indices such as the ionized He fraction to crude but commonly used indices such as the [O III]/H $\beta$  ratio.

#### 4.3.1. He Recombination Lines

The fractional ionization of He provides a robust measure of stellar temperature, following methods established originally by Zanstra (1927). Most of the helium in normal H II regions is either neutral or singly ionized, so the relevant diagnostics are the ratios of the He I and H I recombination lines. Figure 9 shows the line ratios He I  $\lambda$ 5876/H $\beta$  and He I  $\lambda$ 6678/H $\alpha$  plotted as functions of stellar temperature. Superimposed are the model relations, based on the stellar atmosphere models of BKG and assuming Case B recombination following Osterbrock (1989). Models are plotted for abundances of 1.0  $Z_{\odot}$  (solid lines) and 0.2  $Z_{\odot}$  (dashed lines), and for ionization parameter  $\log U$  of  $-1.5$  (upper) and  $-4.0$  (lower). Given the relatively narrow range of  $U$  in our sample the ionization parameter dependence is unimportant, but the range of abundance in the sample has some effect on the observed line ratios (both via line blanketing in the ultraviolet and the He abundance). The symbols differentiate between calibrating single-star regions, and larger Galactic and Magellanic Cloud H II regions, following Figure 4. The model lines represent the mean He ionization over the entire nebula, so for the H II regions with partial He ionization we only considered objects for which we had full or representative spatial coverage of the nebula.

Figure 9 shows an excellent agreement between the observed levels of He ionization and the model predictions, especially for He I  $\lambda$ 6678/H $\alpha$  where our data are the best and reddening errors are minimal. The most discrepant regions are S275, where our spatial coverage is very incomplete,

and S162 (NGC 7635), which is ionized by an O6.5 IIIIf star. The latter is the only H II region in our sample which is predominantly ionized by a giant star, but it is unclear whether the discrepancy for this object is coincidental or indicative of a general problem with the low-gravity stellar models. Otherwise the data show that the He I lines provide an excellent measure of stellar temperature. Unfortunately this method is only sensitive when nebular He is partially ionized ( $35000 \text{ K} \leq T_{\text{eff}} \leq 39000 \text{ K}$ ). Most extragalactic H II regions show nearly complete ionization of helium ( $T_{\text{eff}} \geq 40000 \text{ K}$ ), but the He I lines do provide important constraints on the ionizing spectrum in the innermost metal-rich disks of spirals, where many other hardness indices break down (BKG). Moreover, Fig. 9 provides independent confirmation of the reliability of the Vacca et al. (1996) effective temperature scale, at least for luminosity class V stars in the  $T_{\text{eff}} = 34000 - 39000 \text{ K}$  range.

#### 4.3.2. *Forbidden-Line Excitation Indices*

The simplest and crudest indicators of stellar temperature are based on single forbidden-line ionization indices, such as  $[\text{O III}]/\text{H}\beta$  (Chopinnet & Lortet-Zuckermann 1976, Kaler 1978, Copetti, Pastoriza, & Dottori 1985, 1986), or analogous infrared indices such as  $[\text{O III}] 88 \mu\text{m}/\text{H} 53\alpha$  or  $[\text{N III}] 57 \mu\text{m}/\text{H} 53\alpha$  (Puxley et al. 1989). Figure 10 shows the dependence of  $[\text{O III}] \lambda\lambda 4959, 5007/\text{H}\beta$  on stellar temperature, again with the H II regions subdivided as in Figure 4. This measure of the excitation shows a tight correlation with  $T_{\text{eff}}$  (for this sample of H II regions), confirming the good correlations seen previously by Chopinnet & Lortet-Zuckermann (1976), Kaler (1978), and Hunter (1992). A roughly linear, increasing trend in  $[\text{O III}]/\text{H}\beta$  with  $T_{\text{eff}}$  is expected, because the nebular volume containing double-ionized oxygen increases with the higher ionizing flux emitted by earlier spectral type stars (Stasińska 1978). The observed correlation has a remarkably linear form, extending to the WR stars with temperatures of nearly 70000 K. The adopted  $T_{\text{eff}}$  scale for the WR stars (Esteban et al. 1993) is partly based on nebular modeling, however, so strictly speaking the empirical relation in Fig. 10 only applies for  $T_{\text{eff}} \leq 50000 \text{ K}$ .

Despite the tightness of the correlation in Figure 10, the  $[\text{O III}]/\text{H}\beta$  ratio must be applied with considerable caution to extragalactic H II regions and starbursts, because the ratio is sensitive to other variables such as ionization parameter and metal abundance. This is illustrated by the four model sequences in Fig. 10, plotted for oxygen abundances of  $0.2 Z_{\odot}$  and  $1.0 Z_{\odot}$  and  $\log U = -2.0$  and  $-4.0$  (with  $T_{\text{eff}}$  varying along each sequence). The best fitting models correspond to typical ionization parameters of  $\log U \sim -2.5$  and  $Z/Z_{\odot} \sim 0.5 - 1$ , consistent with the measured values from Fig. 5 and Table 1, respectively. However the same excitation vs  $T_{\text{eff}}$  relation may not apply in external galaxies, where both  $Z/Z_{\odot}$  and  $\log U$  may be shifted relative to the typical values in this sample.

We have also investigated the behavior of two other ionization indices which have been suggested as hardness indicators,  $[\text{Ar III}] \lambda 7135/\text{H}\alpha$  and  $[\text{Ne III}] \lambda 3869/[\text{O II}] \lambda 3727$ . Both are plotted against stellar temperature in Figure 11. The figure also shows the temperature dependence of

[O III]  $\lambda\lambda 4959, 5007/\text{H}\beta$ , but plotted this time with a logarithmic scale to provide a direct comparison with the other two indices. The behavior of [Ar III]/ $\text{H}\alpha$  is qualitatively similar to that seen for [O III]/ $\text{H}\beta$ , but with a larger scatter and shallower slope above  $T_{\text{eff}} \sim 38000$  K. This is not surprising because the lower ionization potential for  $\text{Ar}^+$  (27.6 eV vs 35.1 eV for  $\text{O}^+$ ) is close to the  $\text{He}^+$  edge at 24.6 eV. Furthermore the excitation of [Ar III] is sensitive to the ionization parameter and abundance in the same way as [O III], so it provides a poor substitute for the much more robust  $\text{He}^+/\text{H}^+$  index discussed earlier.

The bottom panel of Fig. 11 shows the temperature dependence of the hybrid forbidden-line ratio [Ne III]  $\lambda 3869$ /[O II]  $\lambda 3727$ . Ali et al. (1991) have shown that this ratio provides a valuable index for deriving ionization correction factors in nebular abundance measurements. Figure 11 shows a strong monotonic dependence of [Ne III]/[O II] on  $T_{\text{eff}}$ , which reflects the 41.1 eV ionization potential of  $\text{Ne}^+$ , but the large scatter in the relation limits its usefulness as a stellar thermometer. The weakness of the [Ne III] line in metal-rich H II regions also limits its value for extragalactic applications. A similar plot of [Ne III]/ $\text{H}\beta$  shows a nearly identical scatter, so variations on [O II] excitation are not responsible for this dispersion. Our result is somewhat surprising in light of the relatively robust behavior of [Ne III]/ $\text{H}\beta$  in the recent analysis of Oey et al. (2000). Of all of the forbidden-line ratios that are accessible at visible wavelengths, the familiar [O III]/ $\text{H}\beta$  index appears to be the most useful stellar temperature indicator, though this sensitivity is accompanied by strong dependences on many other nebular properties.

#### 4.3.3. Composite Ionization Indices: $\eta'$

The well-known sensitivity of excitation indices such as [O III]/ $\text{H}\beta$  to nebular ionization structure and abundance led Mathis (1985) and Vílchez & Pagel (1988) to investigate the use of composite indices based on the ionization of more than one element, in an effort to find a more robust UV hardness indicator. The advent of CCD spectrographs has made the [S III]  $\lambda\lambda 9069, 9532$  doublet accessible, and with it the possibility of using the  $\text{O}^+/\text{O}^{++}$  and  $\text{S}^+/\text{S}^{++}$  to constrain  $T_{\text{eff}}$  independently of metal abundance and ionization parameter. A convenient hardness index is the parameter  $\eta'$  introduced by Vílchez & Pagel (1988):

$$\eta' = \frac{[\text{O II}] \lambda\lambda 3726, 3729 / [\text{O III}] \lambda\lambda 4959, 5007}{[\text{S II}] \lambda\lambda 6716, 6731 / [\text{S III}] \lambda\lambda 9069, 9532}. \quad (2)$$

The robustness of  $\eta'$  can be tested directly by plotting the behavior of [O II]/[O III] vs [S II]/[S III] for 30 Doradus, Orion, and Carina, where we have spectra at multiple positions. This is shown in Figure 12a, along with a series of nebular models from BKG. Constant  $T_{\text{eff}}$  lines are drawn at  $Z = 0.5 Z_{\odot}$  for  $T_{\text{eff}} = 50000, 45000, 40000,$  and  $35000$  K (left to right). Along each line the ionization parameter varies from  $\log U = -1.5$  (bottom) to  $\log U = -4.0$  (top). The dashed lines show the effects of changing metal abundance between  $Z = 0.2 Z_{\odot}$  (left) and  $1.0 Z_{\odot}$  (right, indicated by small dots), for the same range of stellar temperatures and a fixed ionization parameter  $\log U = -2.5$ .

For further details on the models see BKG.

For  $40000 \text{ K} \leq T_{\text{eff}} \leq 50000 \text{ K}$  the lines of constant stellar temperature have a slope of near unity in this diagram (i.e. constant  $\eta'$ ), demonstrating the robustness of  $\eta'$  against changes in ionization parameter, at least in the models. More impressive yet is the distribution of the observed line ratios at the various positions in 30 Doradus (open stars) and Orion (open circles), which fall on lines of nearly constant  $\eta'$ , over ranges of nearly an order of magnitude in  $[\text{O II}]/[\text{O III}]$  or  $[\text{S II}]/[\text{S III}]$ . The observations of Carina (triangles) show a large scatter in  $\eta'$ , and we suspect that this dispersion is real, reflecting the influence of ionization from stars with different temperatures across this complex region. However Oey et al. (2000) have also found that  $\eta'$  shows a larger point-to-point variation in their sample of 4 LMC shell H II regions, and this may suggest limits to the range of spatial scales and nebular properties where  $\eta'$  provides a reliable measure of ionizing stellar temperature.

Although the spectra of 30 Dor and Orion are consistent with a nearly constant value of  $\eta'$  (and hence  $T_{\text{eff}}$ ), Fig. 12a shows a systematic offset between the effective temperatures implied by the models ( $\sim 39000 \text{ K}$  and  $37000\text{--}38000 \text{ K}$  respectively), and those estimated from the stellar contents of the regions ( $\sim 48500 \text{ K}$  and  $40000 \text{ K}$  respectively). Figure 12b shows the same diagram for the other H II regions in the sample (a nebular model for  $T_{\text{eff}} = 30000 \text{ K}$  is added), and a similar offset in the stellar temperature scales is apparent, if one compares with the actual  $T_{\text{eff}}$  values in Table 1. The H II regions ionized by cooler stars ( $T_{\text{eff}} < 37000 \text{ K}$ ) seem to show better agreement with the models. Nevertheless the general consistency between the nebular and spectroscopic temperatures is encouraging, confirming and extending earlier results by Mathis & Rosa (1991).

Figure 12 impressively demonstrates the robustness of  $\eta'$  against systematic variations in  $U$ , but the models plotted in the figure suggest a significant dependence of  $\eta'$  on metal abundance. The dashed lines show the effects of changing  $Z$  from  $0.2 Z_{\odot}$  (left) to  $1.0 Z_{\odot}$  (right). The  $Z$ -dependence is relatively weak for hotter stars ( $T_{\text{eff}} \geq 40000 \text{ K}$ ) and low abundances ( $Z \leq 0.5 Z_{\odot}$ ), but becomes large for cooler stars, where the effects of abundance and stellar temperature become virtually degenerate, and  $\eta'$  itself becomes nearly degenerate with  $[\text{O II}/\text{O III}]$  and  $[\text{O III}]/\text{H}\beta$ . Inspection of the models suggests that two physical effects contribute to this abundance sensitivity, increased stellar metal line blanketing in the ultraviolet, which softens the ionizing spectrum at a given effective temperature, and the increasing dominance of nebular cooling (especially  $\text{O}^{++}$ ) over ionization structure in determining the relative forbidden-line strengths at high abundance (Shields & Searle 1978, Oey & Kennicutt 1993, Stasinska & Leitherer 1996). Thus it is important to confirm the  $\eta'$ -derived stellar temperatures for low-excitation nebulae with those derived from more robust hardness indices, such as the He recombination lines.

The degeneracy between abundance and stellar temperature in model spectra has hampered previous model-based studies of the metallicity dependence of the stellar temperatures and IMFs of extragalactic H II regions (e.g., BKG). However the data presented in this paper allow to test the correlation between  $\eta'$  and  $T_{\text{eff}}$  empirically, independently of the nebular models. The results are shown in Figure 13; the points show the measured values of  $\log \eta'$  and  $T_{\text{eff}}$ , subdivided as in

Fig. 4, while the three lines show the nebular model relations for 0.2, 0.5, and 1.0  $Z_{\odot}$  ( $\log U = -2.5$  in all three cases). The H II regions span a range of roughly 2 dex in  $\log \eta'$  (S237, with no detected [O III] emission, is not plotted), and the index shows a monotonic dependence on stellar temperature, albeit with a considerable scatter. The general shape of the  $\log \eta'$  vs  $T_{eff}$  relation is consistent with that predicted by the nebular models; the hatched line shows a quadratic fit to the observed H II regions (excluding the WR nebulae, where the temperature calibration is uncertain), and its general shape is in good agreement with the model relations for the relevant abundance range of  $\sim 0.4$ – $1.0 Z_{\odot}$ .

In contrast to the behavior of our nebular models, our H II region data show no evidence for a strong  $Z$ -dependence of the  $\eta'$  vs  $T_{eff}$  relation. In particular, there is no evidence in Fig. 13 for a systematic shift between the LMC H II regions and the more metal-rich (on average) Galactic H II regions, or likewise for any difference between the most metal-rich and metal-poor Galactic H II regions. Within the considerable scatter the trends seen in Fig. 13 are independent of abundance. The singular exception of the SMC H II region N66, which is the most metal-poor region in the sample, but the  $T_{eff}$  value of this region almost certainly is underestimated, due to the presence of the luminous WR star HD 5980 (see the appendix).

We cannot explain why the observed behavior of  $\eta'$  appears to be more robust than the models would predict, but we can speculate on the possible reasons. As pointed out earlier, our empirical estimates of  $T_{eff}$  for the H II regions are based on stellar spectral classifications, using a single, metallicity-independent spectral type vs  $T_{eff}$  calibration (Vacca et al. 1996). We believe that this procedure is justified, because the stellar types are predominantly assigned on the basis of H, He<sup>0</sup>, and He<sup>+</sup> absorption line strengths, which ought be robust against metallicity effects. However the stellar atmosphere grids which are used in the nebular models do show considerable changes in ultraviolet line blanketing with increasing metal abundance, and this may alter the ionization temperature at a given fixed effective temperature, in a way that would not be reflected in the assigned spectral types of the stars. Stated in another way, although we have calibrated  $\eta'$  in terms of stellar effective temperatures in Figure 13, the ionization temperatures that are derived from  $\eta'$  may not necessarily coincide with  $T_{eff}$  for abundances that differ substantially from the local Galactic value. We return to this point in §5.

In summary, our data suggest that  $\eta'$  offers the prospect of estimating the characteristic stellar temperatures of the ionizing associations in H II regions, over a relatively large temperature range ( $33000K \leq T_{eff} < 50000K$ ), and on a calibration that is directly tied to the stellar spectral classification system, independent of the nebular model chain. However two important limitations of  $\eta'$  must be recognized before the results in Fig. 13 are applied indiscriminantly to H II regions in external galaxies. First, the scatter in the  $\log \eta'$  vs  $T_{eff}$  relation is considerable, amounting to an rms uncertainty of  $\pm 3000$  K for any individual region. Second, photoionization models suggest that abundance effects may introduce systematic shifts of a comparable magnitude in the derived effective temperatures, though the observations of the calibrating H II regions do not show evidence for shifts of this magnitude.



## 5. Application to Extragalactic H II Regions

In this section we briefly apply the empirical relations between nebular hardness properties and stellar temperature from the previous section to the sample of extragalactic H II regions studied by BKG. The BKG data are well suited to our purposes because they span a large range of metal abundance and spiral galaxy type, and they are based on spectra covering the 3600–9700 Å range, so we can apply all of the hardness indices discussed earlier, including  $\eta'$ . Our approach is complementary to the model-based studies of Vílchez & Pagel (1988), Stasińska & Leitherer (1996), and BKG.

We begin by using the empirical fit to the  $\log \eta'$  vs  $T_{eff}$  relation in Fig. 13 (hatched line) to derive stellar temperatures for the BKG extragalactic H II regions with reliable measurements of  $\eta'$ . Fitting a quadratic function to the calibrating Galactic H II regions (solid squares) yields:

$$T_{eff} = 50819 - 16485x + 3778x^2 \quad (3)$$

where  $x \equiv \log \eta'$ . Although this relation is based solely on the smaller calibrating H II regions, where the  $T_{eff}$  values are the most reliable, using the entire sample does not change the resulting relation significantly. Equation (3) is given primarily so readers can reproduce and check the results described below; in view of the caveats discussed in the previous section we *strongly* advise against applying this relation generally to extragalactic regions, least of all to luminous starbursts, where the physical conditions may differ substantially from those of the calibrating H II regions.

With these caveats firmly in mind, the top panel of Figure 14 shows the characteristic stellar temperatures  $T_*$  and oxygen abundance for the BKG sample. We have deliberately avoided referring to these as effective temperatures, to emphasize that these are ionization temperatures which may not coincide precisely with  $T_{eff}$  outside the calibrated abundance range. The abundances have been derived using the  $R_{23}$  empirical method following the calibration of Edmunds & Pagel (1984), and should be reliable to within  $\pm 0.2$  dex for  $Z \leq Z_\odot$ , but less accurate at higher abundances. However this accuracy is sufficient for testing for general trends in  $T_*$  with metallicity. The values of  $T_*$  inferred from equation (3) show a large scatter, consistent with the large scatter observed in the calibrating sample (Fig. 13), combined with any real scatter in  $T_*$  at fixed abundance, due to variations in age and other properties of the ionizing star clusters. The large dispersion in Fig. 14a underscores the dangers of applying  $\eta'$  or any other forbidden-line hardness parameter to an individual H II region. Nevertheless the general behavior of  $T_*$  should be meaningful.

The top panel of Fig. 14 shows a clear trend in stellar temperature, with the typical  $T_{eff}$  decreasing from  $\sim 55000$  K at  $0.2 Z_\odot$  ( $12 + \log O/H = 8.2$ ) to  $\sim 40000$  K above solar abundance ( $12 + \log O/H = 8.9$ ). This trend is in excellent agreement with the model-based results of BKG, except for a temperature offset of about 5000 K; BKG estimated a  $T_{eff}$  range of 50000 K to 35000 K over the same abundance range. In both cases note that most of the  $T_{eff}$  change is restricted to abundances below solar.

The measured He I line strengths in the BKG spectra provide another empirical constraint on

the stellar temperatures in metal-rich H II regions. Unfortunately the He lines are only useful for regions ionized by stars with  $T_{eff} \leq 38000$  K, when one allows for observational uncertainties in the He line fluxes and the dependences on abundance and ionization parameter. Nevertheless we can at least test the consistency of the  $\eta'$  and  $\text{He}^+/\text{He}^0$  temperature scales for the most metal-rich regions ( $12 + \log O/H > 9.0$ ). The crosses in Fig. 14 show the values of  $T_{eff}$  that are implied by the observed  $\text{He I } \lambda 5876/\text{H}\beta$  ratios and the models shown in Fig. 9 (the  $\text{He I } \lambda 6678$  line is usually too faint to provide reliable constraints on  $T_{eff}$ ), with arrows indicating objects for which the He recombination lines only set lower limits on  $T_{eff}$ . The He I data confirm the general trend toward lower  $T_*$  for  $Z > Z_\odot$ , but with  $T_* \sim 38000 - 39000$  K at the highest abundances, about 2000 K cooler than given by  $\eta'$ . This comparison provides a good illustration of how two different hardness indices can provide complementary constraints on the stellar populations in the H II regions.

As an additional consistency check on these results, the bottom panel of Fig. 14 shows the same relation, but in this case with the  $T_*$  values derived from the average of the  $\eta'$  vs  $T_{eff}$  calibration (Fig. 13 and eq. [3]), and the relation between  $[\text{O III}]/\text{H}\beta$  and  $T_{eff}$  from Fig. 10). The latter is known to be sensitive to ionization parameter and to metal abundance itself, but surprisingly it yields values of  $T_*$  that are close to those derived from  $\eta'$ . This comparison yields a somewhat lower  $T_*$  values at high abundance, which are in better agreement with the values derived from the He I recombination lines. However because of the susceptibility of  $[\text{O III}]/\text{H}\beta$  to dependences on parameters other than  $T_{eff}$  we do not apply this diagnostic further. We suspect that the general consistency of the results here are due to the fact that mean abundances and ionization parameters of the calibrating H II region samples are typical of the extragalactic H II regions in the BKG sample, but this does *not* imply that the abundance dependence of  $T_*$  implied by the  $[\text{O III}]$  excitation is necessarily robust by any means.

In summary the empirically-based stellar temperature indices show evidence for a systematic decrease in mean stellar temperature with increasing metal abundance, which appears to qualitatively confirm previous results based on nebular model fitting (Vílchez & Pagel 1988, BKG). Several physical effects can contribute to this softening of the ionizing continuum with increasing metallicity: increased line blanketing at constant  $T_{eff}$ , a shift in  $T_{eff}$  at constant stellar mass, and/or a change in the upper mass limit to the IMF. The models of Stasínska & Leitherer (1996) suggest that changes in atmospheric blanketing and stellar evolution can account for most of the changes, and our results do not contradict this conclusion. We refer the reader to that paper and to BKG for a more complete discussion of the implications of these changes in  $T_{eff}$ .

## 6. CONCLUSIONS

In conclusion, we have presented a set of empirical diagnostic line ratios, calibrated against the effective temperature of the exciting stars. Our results provide a stronger empirical foundation for many of the most widely used nebular diagnostics (e.g.,  $R_{23}$ ,  $\eta'$ ), and they show much better agreement between observations and models than often was seen in earlier generations of stellar

atmosphere and nebular photoionization models (cf., Mathis 1985, Vílchez & Pagel 1988). The empirical relations presented here should be useful in many investigations of the stellar populations of extragalactic H II regions, where very limited information is available on the exciting stars, and where an estimate of the nebular-based effective temperature is needed, even with a restricted wavelength coverage.

We close by reemphasizing the exploratory nature of this study, and pointing out the most urgently needed improvements before one can reliably extract quantitative constraints on the stellar contents and IMFs of star forming regions from nebular spectra. On the empirical side, this approach can be much improved if accurate ( $T_e$ -based) metal abundances are obtained for all of the calibrating H II regions (or their exciting stars), and the effects of effective temperature, metal abundance, and nebular geometry are accounted for explicitly in the analysis. Oey et al. (2000) have demonstrated the value of obtaining high signal/noise point-by-point measurements of individual H II regions, and applying this approach to a larger sample of objects would provide a major improvement over our exploratory analysis. On the theoretical side, more self-consistent stellar models for the relevant range of abundances, temperatures, and gravities are the most crucial inputs. This would also allow for a consistent treatment of stellar and nebular abundances in the photoionization calculations. We hope that these initial results may stimulate further progress in these areas.

It is a pleasure to thank A. Pauldrach, R.-P. Kudritzki, and T. Hoffmann for sharing their unpublished stellar atmosphere models, and S. Oey for a preliminary version of her paper and many discussions about this work. This research was supported in part by the National Science Foundation through grants AST-9421145 and AST-9900789.

## APPENDIX EXPLANATORY NOTES ON INDIVIDUAL H II REGIONS

S257: The spectral type adopted is the one predicted by HM90 on the basis of the observed total nebular ionizing flux.

S275 (Rosette): The ionizing cluster is NGC 2244; earliest spectral type is O4 V((f)); a total of 9 stars earlier than B0.5 has been included in the computation of  $T_{eff}$ .

RCW 5 (NGC 2359): A Wolf-Rayet (WN 4) ring nebula. Esteban et al. (1993) derive  $T_{eff}=67\pm 11 \times 10^4 K$ . Given the uncertainties in the treatment of WR star atmospheres, this object, together with RCW 48, is included to observe the trends in the nebular diagnostics at very high  $T_{eff}$  values.

RCW 16: Walborn (1982) gives two early-type stars in NGC 2467, HD 64568 (O3 V((f\*))) and HD 64315 (O6 Vn).

RCW 48 (NGC 3199): The second Wolf-Rayet (WN 5) ring nebula in our sample, with  $T_{eff}=57\pm 14 \times 10^4 K$  (Esteban et al. 1993).

RCW 53 (Carina): A total of 36 early-type stars in Tr14 and Tr16 has been considered, excluding  $\eta$  Carinae and one WR star (HD 93162).

RCW 57 (NGC 3603): Drissen et al. (1995) identify 11 O-type stars and 3 WN6 stars which account for at least 80% of the ionization of the nebula. The temperature derived here does not include the WN6 stars, which according to Esteban et al. (1993) have  $T_{eff} \leq 42000$  K.

S49 (M16): 20 early-type stars

S45 (M17): 12 early-type stars classified from optical and  $K$ -band spectroscopy by Hanson, Howarth & Conti (1997).

S100: The spectral type adopted is the one predicted by HM90 on the basis of the observed total nebular ionizing flux.

S158 (NGC 7538): Ionizing star is CGO 654, with spectral type O7V, from Crampton, Georgelin, & Georgelin (1978).

S162 (NGC 7635): Ionizing star is BD+60 2522, with spectral type O6.5 IIIf, from Conti & Alschuler (1971). Classified as O6.5 IIIef by Conti & Leep (1974).

N11B: We have assumed that the stellar association LH10 is responsible for the ionization (26 ionizing stars).

N44: The slit was centered on N44B, ionized by LH 47/48.

N51D: We have included the 40 early-type stars classified by Oey & Smedley (1998) in LH 51 and LH 54.

N144: Garmany, Massey & Parker (1994) list 32 ionizing stars in LH 58. The 3 WR stars were not included.

30 Dor: We have included the 64 early-type stars in R136 listed by Massey & Hunter (1998), excluding the WR stars.

N70: The ionizing cluster is LH 114, studied by Oey (1996).

N180: The ionizing cluster has been assumed to be LH 117, studied by Massey et al. (1989a).

N66 (SMC): The temperature we derived is based on the stellar census of Massey et al. (1989). However the calculation does not include the peculiar WN3+OB binary HD 5980, which according to Massey et al. could account for up to half of the ionization of the nebula. Consequently the temperature listed in Table 1 is strictly a lower limit.

## REFERENCES

- Ali, B., Blum, R.D., Bumgardner, T.E., Cranmer, S.R., Ferland, G.J., Haefner, R.I., & Tiede, G.P. 1991, *PASP*, 103, 1182
- Alloin, D., Collin-Soufrin, S., Joly, M., & Vigroux, L. 1979, *A&A*, 78, 200
- Baldwin, J.A., Phillips, M.M., & Terlevich, R. 1981, *PASP*, 93, 5
- Baldwin, J.A., & Stone, R.P.S. 1984, *MNRAS*, 206, 241
- Bresolin, F., Kennicutt, R.C., & Garnett, D. R. 1999, *ApJ*, 510, 104
- Cardelli, J. A., Clayton, G. C., & Mathis, J. S. 1989, *ApJ*, 345, 245
- Chopinnet, M., & Lortet-Zuckermann, M.C. 1976, *A&AS*, 25, 179
- Chopinnet, M., Georgelin, Y.M., & Lortet-Zuckermann, M.C. 1973, *A&A*, 29, 225
- Crampton, D., Georgelin, Y. M., & Georgelin, Y. P. 1978, *A&A*, 66, 1
- Conti, P. S., & Alschuler, W. R. 1971, *ApJ*, 170, 325
- Conti, P. S., & Leep, E. M. 1974, *ApJ*, 193, 113
- Copetti, M.V., Pastoriza, M.G., & Dottori, H.A. 1985, *A&A*, 152, 427
- Copetti, M.V., Pastoriza, M.G., & Dottori, H.A. 1986, *A&A*, 156, 111
- Díaz, A. I., Terlevich, E., Pagel, B. E. J., Vílchez, J. M., & Edmunds, M. G. 1987, *MNRAS*, 226, 19
- Díaz, A. I., Terlevich, E., Vílchez, J. M., Pagel, B. E. J., & Edmunds, M. G. 1991, *MNRAS*, 253, 245
- Díaz, A. I., & Pérez-Montero, E. 1999, *MNRAS*, in press
- Dinerstein, H.L. 1996, in *ASP Conf. Ser. 99, Cosmic Abundances*, ed. S.S. Holt & G. Sonneborn (San Francisco: ASP), 337
- Drissen, L., Moffat, A.F.J., Walborn, N.R., & Shara, M.M. 1995, *AJ*, 110, 2235
- Dufour, R.J. 1975, *ApJ*, 195, 315
- Dutil, Y., & Roy, J.-R. 1999, *ApJ*, 516, 62
- Edmunds, M.G., & Pagel, B.E.J. 1984, *MNRAS*, 211, 507
- Esteban, C., Smith, L.J., Vilchez, J.M., & Clegg, R.E.S. 1993, *A&A*, 272, 299
- Evans, I. N., & Dopita, M. A. 1985, *ApJS*, 58, 125
- Ferland, G. J., Korista, K. T., Verner, D. A., Ferguson, J. W., Kingdon, J. B., & Verner, E. M. 1998, *PASP*, 110, 761
- García-Vargas, M. L., González-Delgado, R. M., Pérez, E., Alloin, D., Díaz, A., & Terlevich, E. 1997, *ApJ*, 478, 112
- Garmany, C.D., Massey, P., & Parker, J.W. 1994, *AJ*, 108, 1256

- Garnett, D.R. 1999, in IAU Symposium 190, New Views of the Magellanic Clouds, ed. Y.-H. Chu, N. Suntzeff, J. Hesser, & D. Bohlender, (San Francisco: ASP), in press
- Garnett, D.R. 2000, in Spectrophotometric Dating of Stars and Galaxies, ed. I. Hubeny, S. Heap, & R. Cornett (San Francisco: ASP), in press
- Georgelin, Y.M., Georgelin, Y.P., & Roux, S. 1973, *A&A*, 25, 337
- Hanson, M.M., Howarth, I.D., & Conti, P.S. 1997, *ApJ*, 489, 698
- Heydari-Malayeri, M. 1988, *A&A*, 202, 240
- Hillenbrand, L. A., Massey, P., Strom, S.E., & Merrill, K.M. 1993, *AJ*, 106, 1906
- Hummer, D.G., & Storey, P.J. 1987, *MNRAS*, 224, 801
- Hunter, D.A. 1992, *ApJS*, 79, 469
- Hunter, D.A., & Massey, P. 1990, *AJ*, 99, 846 (HM90)
- Kaler, J.B. 1978, *ApJ*, 220, 887
- Kaler, J. B., & Jacoby, G. H. 1989, *ApJ*, 345, 871
- Kennicutt, R.C. 1984, *ApJ*, 287, 116
- Lada, C.J., Gull, T.R., Gottlieb, C.A., & Gottlieb, E.W. 1976, *ApJ*, 203, 159
- Lahulla, J.F. 1987, *AJ*, 94, 1062
- Leitherer, C., & Heckman, T. 1995, *ApJS*, 96, 9L
- Leitherer, C. et al. 1999, *ApJS*, 123, 3
- Massey, P., Garmany, C.D., Silkey, M., & DeGioia-Eastwood, K. 1989a, *AJ*, 97, 107
- Massey, P., & Hunter, D.A. 1998, *ApJ*, 493, 180
- Massey, P., & Johnson, J. 1993, *AJ*, 105, 980
- Massey, P., Johnson, K.E., & DeGioia-Eastwood, K. 1995, *ApJ*, 454, 151
- Massey, P., Parker, J.W., & Garmany, C.D. 1989b, *AJ*, 98, 1305
- Massey, P., Strobel, K., Barnes, J.V., & Anderson, E. 1988, *ApJ*, 328, 315
- Mathis, J. S. 1985, *ApJ*, 291, 247
- Mathis, J. S., Chu, Y.-H., & Peterson, D. E. 1985, *ApJ*, 292, 155
- Mathis, J. S., & Rosa, M. R. 1991, *A&A*, 245, 625
- McCall, M. L., Rybski, P. M., & Shields, G. A. 1985, *ApJS*, 57, 1
- Melnick, J., Tapia, M., & Terlevich, R. 1989, *A&A*, 213, 89
- Oey, M.S. 1996, *ApJ*, 465, 231
- Oey, M.S., & Kennicutt, R.C. 1993, *ApJ*, 411, 137
- Oey, M.S., & Massey, P. 1995, *ApJ*, 452, 210

- Oey, M.S., & Smedley, S.A. 1998, *AJ*, 116, 1263
- Oey, M.S., Dopita, M.A., Shields, J.C., & Smith, R.C. 2000, *ApJ*, submitted
- Oke, J. B., & Gunn, J. E. 1983, *ApJ*, 266, 713
- Osterbrock, D. E. 1989, *The Astrophysics of Gaseous Nebulae and Active Galactic Nuclei* (Mill Valley, CA: University Science Books)
- Pagel, B. E. J., Edmunds, M. G., Blackwell, D. E., Chun, M. S., & Smith, G. 1979, *MNRAS*, 189, 95
- Pagel, B.E.J., & Edmunds, M.G. 1978, *MNRAS*, 185, 77
- Parker, J.W., Garmany, C.D., Massey, P., & Walborn, N.R. 1992, *AJ*, 103, 1205
- Pauldrach, A. W. A., Lennon, M., Hoffmann, T. L., Sellmaier, F., Kudritzki, R.-P., & Puls, J. 1998, *Second Boulder-Munich Workshop on Hot Stars*, p. 258
- Peimbert, M., & Torres-Peimbert, S. 1977, *MNRAS*, 179, 217
- Peimbert, M., Torres-Peimbert, S., & Dufour, R.J. 1993, *ApJ*. 418
- Puxley, P. J., Brand, P. W. J. L., Moore, T. J. T., Mountain, C. M., Nakai, N., & Yamashita, T. 1989, *ApJ*, 345, 163
- Rieke, G.H., Loken, K., Rieke, M.J., & Tamblyn, P. 1993, *ApJ*, 412, 99
- Roy, J.-R., & Roy, J.R. 1997, *MNRAS*, 288, 715
- Ryder, S. D. 1995, *ApJ*, 444, 610
- Schaerer, D., & de Koter, A., 1997, *A&A*, 322, 598
- Searle, L. 1971, *ApJ*, 168, 327
- Shaver, P.A., McGee, R.X., Newton, L.M., Danks, A.C., & Pottasch, S.R. 1983, *MNRAS*, 204, 53
- Shields, G. A., & Searle, L. 1978, *ApJ*, 222, 821
- Shields, G. A. 1990, *ARA&A*, 28, 525
- Stasińska, G. 1978, *A&AS*, 32, 429
- Stasińska, G., & Leitherer, C. 1996, *ApJS*, 107, 661
- Stone, R.P.S., & Baldwin, J.A. 1983, *MNRAS*, 204, 347
- Talent, D. L., & Dufour, R. J. 1979, *ApJ*, 233, 888
- Vacca, W. D., Garmany, C. D., & Shull, J. M. 1996, *ApJ*, 460, 914
- Vila-Costas, M.B., & Edmunds, M.G. 1992, *MNRAS*, 259, 121
- Vílchez, J. M., & Pagel, B. E. J. 1988, *MNRAS*, 231,257
- Vílchez, J. M., & Esteban, C. 1996, *MNRAS*, 280, 720
- Walborn, N.R. 1982, *AJ*, 87, 1300

Walborn, N.R. 1987, AJ, 93, 868

Zanstra, H. 1927, ApJ, 65, 50

Zaritsky, D., Kennicutt, R. C., & Huchra, J. P. 1994, ApJ, 420, 87



## FIGURE LEGENDS

Fig. 1.— Distribution of oxygen abundances and ionization-weighted stellar temperatures for the H II region sample. Open squares denote nebulae with direct abundance determinations based on electron temperature measurements. Filled triangles denote H II regions with empirical ( $R_{23}$ ) abundance estimates.

Fig. 2.— Charts showing the locations of the long-slit spectrophotometric measurements. In all cases north is at the top and east is to the left. The box in M8 (Fig. 2d) indicates the region covered by the drift scan.

Fig. 3.— Diagnostic diagrams showing the differences between the fixed pointing spectra (solid points) and the drift scans (open points) for the northern sample of Galactic H II regions.

Fig. 4.— Comparison of spectral properties of the Galactic calibrating H II regions (solid squares), large Galactic H II regions (open squares), LMC and SMC H II regions (open circles), and WR nebulae (open stars). The small triangles show for comparison the spectral sequence for extragalactic H II regions in a large sample of galaxies from BKG.

Fig. 5.— Relation between  $[\text{O III}]/\text{H}\beta$  and  $[\text{N II}]/\text{H}\alpha$  for the H II regions in this sample, subdivided by stellar effective temperature (left) and by nebular oxygen abundance (right).

Fig. 6.— The  $[\text{S II}]\lambda\lambda 6716, 6731/[\text{S III}]\lambda\lambda 9069, 9532$  vs  $T_{\text{eff}}$  diagram for the H II regions. The symbol coding is the same as in Fig. 4. The continuous lines show nebular models at  $0.2 Z_{\odot}$ , for a variety of ionization parameter values  $\log U$  (as labelled). The dotted lines refer to solar abundance models at  $\log U = -2.0, -2.5$  and  $-3.0$ .

Fig. 7.— (Left): Relation between  $[\text{O III}]/\text{H}\beta$  and  $[\text{O II}]/\text{H}\beta$  for subregions observed in 30 Doradus (open stars), Carina (solid triangles), and Orion (open circles). The dashed lines show constant values of the empirical abundance parameter  $R_{23}$ . Note the relative constancy of  $R_{23}$  across the 30 Dor and Carina, despite the large local variations in excitation. (Right): Corresponding relation between  $[\text{S III}]/\text{H}\beta$  and  $[\text{S II}]/\text{H}\beta$  line ratios. Diagonal lines show constant values of the abundance index  $S_{23}$ .

Fig. 8.— Relation between  $[\text{O III}]/\text{H}\beta$  and the extragalactic H II region empirical abundance index  $[\text{O III}]/[\text{N II}]$ , for subregions observed in 30 Doradus (open stars), Carina (solid triangles), and Orion (open circles). The dashed horizontal lines show values of constant oxygen abundance, using the calibration of Dutil & Roy (1999).

Fig. 9.— Dependence of nebular He I recombination line strengths (relative to Balmer lines) as a function of stellar effective temperature, as measured by He I  $\lambda 5876$  (top) and He I  $\lambda 6678$  (bottom). Both ratios are approximately proportional to the fraction ionization of He in the nebula. Symbols are coded as in Fig. 4. The lines show the relations expected from stellar atmosphere and nebular

photoionization models for different abundances, as described in the text.

Fig. 10.— Correlation between excitation index  $[\text{O III}]/\text{H}\beta$  and stellar effective temperature, with symbols coded as in Fig. 4. The four sets of lines show photoionization model sequences for oxygen abundances of 0.2 and 1.0  $Z_{\odot}$  and ionization parameters  $\log U = -2.0$  and  $-4.0$ .

Fig. 11.— Dependences of three nebular excitation indices on stellar effective temperatures. The symbols are coded as in Figs. 4 and 10.

Fig. 12.— Relationship between ionization-sensitive forbidden-line ratios  $[\text{S II}]/[\text{S III}]$  and  $[\text{O II}]/[\text{O III}]$ . (a) Spatially resolved observations of the 30 Doradus nebula (open circles), the Orion nebula (solid squares), and the Carina nebula (open triangles). The solid lines show photoionization model sequences for stellar temperatures of 50000 K, 45000 K, 40000 K, and 35000 K (left to right). (b) The same line ratios for the full sample of H II regions, with symbols coded as in Fig. 4. Solid lines show the same model sequences, with the addition of a 30000 K model (far right). Dashed lines show the effects of increasing the metal abundance, as discussed in the text.

Fig. 13.— Dependence of the ionization hardness parameter  $\eta'$  (eq. [2]) and stellar effective for the H II regions in this sample, with symbols coded as in Fig. 4. The lines show photoionization model sequences for oxygen abundances of 0.2, 0.5, and 1.0  $Z_{\odot}$ . The hatched line shows a quadratic empirical fit to the data.

Fig. 14.— The top panel shows the relationship between mean stellar temperature inferred from the  $\eta'$  parameter (eqs. [2, 3]) and nebular oxygen abundances, for the BKG sample of extragalactic H II regions. The middle panel shows the stellar temperatures derived from an average of  $\eta'$  and  $[\text{O III}]/\text{H}\beta$ , as described in the text. Crosses in both panels show values of  $T_*$  derived from He I  $\lambda 5876/\text{H}\beta$ . Arrows indicate lower limits to  $T_*$ , corresponding to full He ionization.

Table 1. H II region sample

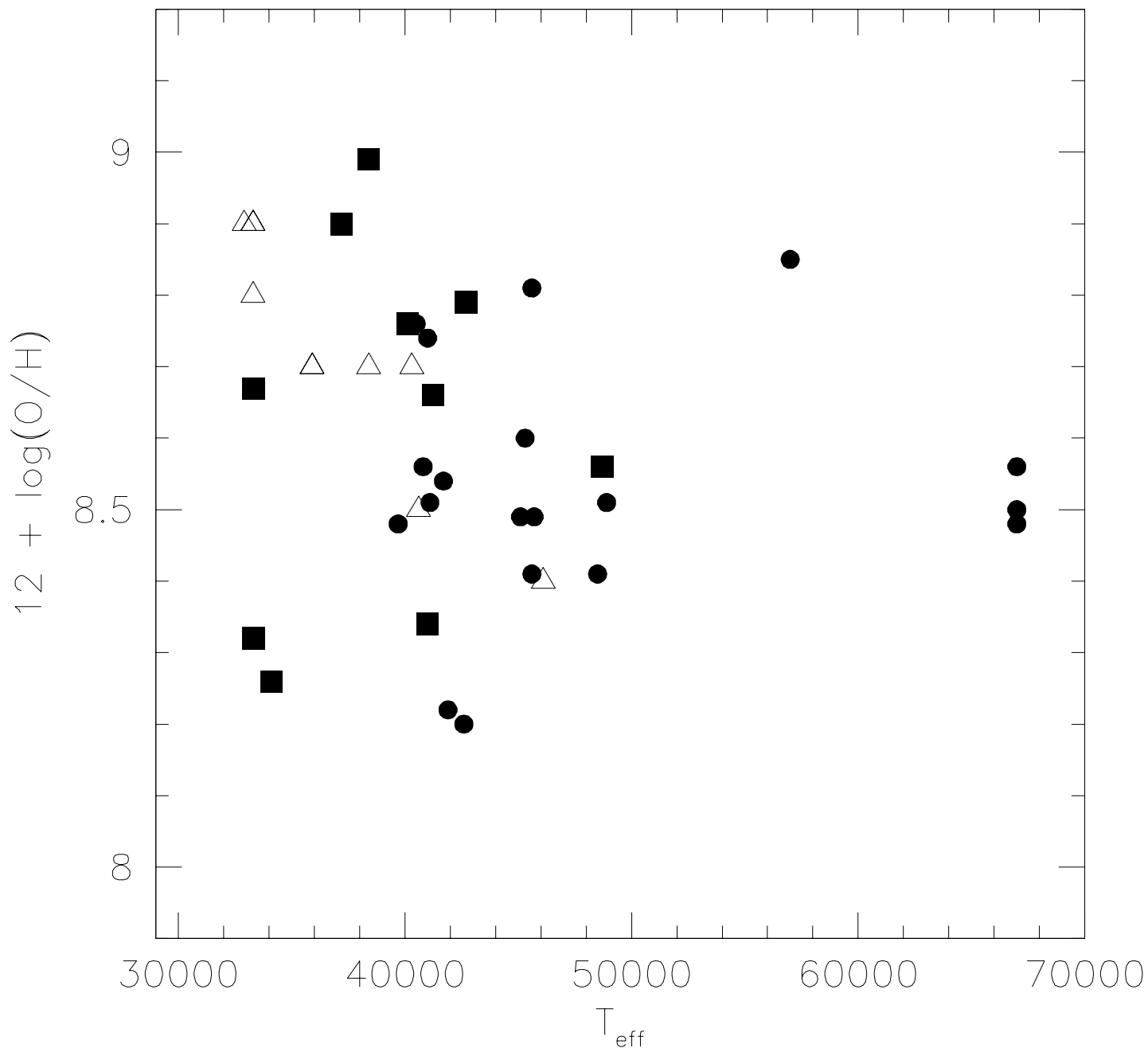
| H II Region<br>(1) | RA (2000)<br>(2) | DEC (2000)<br>(3) | T <sub>*</sub><br>(4) | log Q <sub>0</sub><br>(5) | 12+log(O/H)<br>(6) | Ref.<br>(7) | Tel.<br>(8) | Other ID<br>(9)       |
|--------------------|------------------|-------------------|-----------------------|---------------------------|--------------------|-------------|-------------|-----------------------|
| Galaxy             |                  |                   |                       |                           |                    |             |             |                       |
| S212 *             | 04 40 36         | 50 27 46          | 40600                 | 49.07                     | (8.5)              | 1           | Bok         |                       |
| S237 *             | 05 31 27         | 34 14 58          | 32900                 | 48.21                     | (8.9)              | 1           | Bok         |                       |
| M42 *              | 05 35 17         | -05 23 28         | 40100                 | 49.11                     | 8.76               | 2,a         | CTIO        | Orion, NGC 1976       |
| S255 *             | 06 12 54         | 17 59 23          | 33300                 | 48.02                     | 8.32               | 1,b         | CTIO        | IC 2162               |
| S257 *             | 06 12 48         | 18 00 00          | 34100                 | 48.37                     | 8.26               | 1,b         | Bok         |                       |
| S271 *             | 06 14 59         | 12 20 16          | 33300                 | 48.02                     | (8.9)              | 1           | Bok         |                       |
| S275               | 06 31 40         | 04 57 48          | 42600                 | 49.83                     | 8.20               | 3,b         | CTIO        | Rosette neb.          |
| S288 *             | 07 08 37         | -04 18 48         | 35900                 | 48.46                     | (8.7)              | 1           | Bok         |                       |
| RCW 6 *            | 07 09 54         | -18 30 21         | 42700                 | 49.29                     | 8.79               | 4,b         | CTIO        | S301                  |
| RCW 5              | 07 18 30         | -13 13 48         | 67000                 | 48.90                     | 8.48               | 5,b         | CTIO        | NGC 2359, S298        |
| RCW 8 *            | 07 30 04         | -18 32 13         | 33300                 | 48.32                     | 8.67               | 1,b         | CTIO        | S305                  |
| S307 *             | 07 35 33         | -18 45 34         | 33300                 | 48.02                     | (8.8)              | 1           | Bok         |                       |
| RCW 16 *           | 07 52 19         | -26 26 30         | 48700                 | 49.95                     | 8.56               | 6,b         | CTIO        | NGC 2467, S311        |
| RCW 34 *           | 08 56 28         | -43 05 46         | 37200                 | 48.64                     | 8.90               | 7,b         | CTIO        |                       |
| RCW 40 *           | 09 02 21         | -48 41 55         | 38400                 | 48.80                     | 8.99               | 8,b         | CTIO        |                       |
| RCW 48             | 10 16 33         | -57 56 02         | 57000                 | 49.57                     | 8.85               | 5,b         | CTIO        | NGC 3199              |
| RCW 53             | 10 44 19         | -59 53 21         | 45700                 | 50.91                     | 8.49               | 9,b         | CTIO        | Carina neb., NGC 3372 |
| NGC 3603           | 11 15 09         | -61 16 17         | 48900                 | 50.77                     | 8.51               | 10,b        | CTIO        | RCW 57                |
| RCW 62             | 11 38 20         | -63 22 22         | 41700                 | 50.06                     | 8.54               | 11,b        | CTIO        | λ Cen                 |
| M8                 | 18 03 37         | -24 23 12         | 41000                 | 49.05                     | 8.74               | 12,c        | Bok         | NGC 6523, S25, Lagoon |
| M16                | 18 18 48         | -13 47 00         | 40500                 | 50.21                     | 8.76               | 13,d        | Bok         | NGC 6611, S49, Eagle  |
| M17                | 18 20 26         | -16 10 36         | 45600                 | 50.37                     | 8.81               | 14,a        | Bok         | NGC 6618, S45, Omega  |
| S99 *              | 20 00 54         | 33 29 48          | 38400                 | 48.80                     | (8.7)              | 1           | Bok         |                       |
| S100 *             | 20 01 44         | 33 31 14          | 46100                 | 49.82                     | (8.4)              | 1           | Bok         |                       |
| S148 *             | 22 56 09         | 58 30 00          | 33300                 | 48.02                     | (8.9)              | 1           | Bok         |                       |
| S152 *             | 22 58 40         | 58 47 01          | 35900                 | 48.46                     | (8.7)              | 1           | Bok         |                       |
| S156 *             | 23 05 59         | 60 15 01          | 40300                 | 49.28                     | (8.7)              | 1           | Bok         | IC 1470               |
| S158 *             | 23 13 46         | 61 28 21          | 41000                 | 49.05                     | 8.34               | 8,e         | Bok         | NGC 7538              |
| S162 *             | 23 20 44         | 61 11 41          | 41250                 | 49.47                     | 8.66               | 2,e         | Bok         | NGC 7635, Bubble      |
| LMC                |                  |                   |                       |                           |                    |             |             |                       |
| N11B               | 04 54 49         | -66 25 36         | 45100                 | 50.81                     | 8.49               | 15,b        | CTIO        | DEM 34                |
| N44                | 05 22 06         | -67 55 00         | 40800                 | 50.53                     | 8.56               | 16,b        | CTIO        | DEM 152               |
| N138D,B            | 05 24 23         | -68 31 48         | 67000                 | ...                       | 8.50               | b           | CTIO        | DEM 174               |
| N51D               | 05 26 14         | -67 30 18         | 39700                 | 50.46                     | 8.48               | 17,b        | CTIO        | DEM 192               |
| N144               | 05 26 33         | -68 51 48         | 41100                 | 50.43                     | 8.51               | 18,b        | CTIO        | DEM 199               |
| N57C               | 05 33 10         | -67 42 48         | 67000                 | ...                       | 8.56               | b           | CTIO        | NGC 2020, DEM 231     |
| 30 Dor             | 05 38 42         | -69 06 03         | 48500                 | 51.63                     | 8.41               | 19,d        | CTIO        |                       |
| N70                | 05 43 21         | -67 50 48         | 45300                 | 50.31                     | 8.60               | 20,b        | CTIO        | DEM 301               |
| N180               | 05 48 14         | -70 02 00         | 45600                 | 50.48                     | 8.41               | 21,b        | CTIO        | DEM 322               |
| SMC                |                  |                   |                       |                           |                    |             |             |                       |
| N66                | 00 59 18         | -72 10 48         | 41900                 | 50.72                     | 8.22               | 22,d        | CTIO        | NGC 346               |

References. — Sources of spectral types: 1. Hunter & Massey 1990; 2. Conti & Alschuler 1971; 3. Massey et al 1995; 4. Lahulla 1987; 5. Esteban et al 1993; 6. Walborn 1982; 7. Heydari-Malayeri 1988; 8. Georgelin et al 1973; 9. Massey & Johnson 1993; 10. Drissen et al 1995; 11. Walborn 1987; 12. Lada et al 1976; 13. Hillenbrand et al 1993; 14. Hanson et al 1997; 15. Parker et al 1992; 16. Oey & Massey 1995; 17. Oey & Smedley 1998; 18. Garmany et al 1994; 19. Massey & Hunter 1998; 20. Oey 1996; 21. Massey et al 1989a; 22. Massey et al 1989b.

Sources of abundances: a. Peimbert et al 1993; b. This paper; c. Melnick et al 1989; d. Shaver et al 1983; e. Talent & Dufour 1979.

Table 2. Reddening-corrected line fluxes

| HII Region | c    | [O II]<br>3727 | [Ne III]<br>3869 | [O III]<br>4959+5007 | He I<br>5876 | [N II]<br>6548+6583 | He I<br>6678 | [S II]<br>6716+6731 | [Ar III]<br>7135 | [S III]<br>9069+9532 |
|------------|------|----------------|------------------|----------------------|--------------|---------------------|--------------|---------------------|------------------|----------------------|
| (1)        | (2)  | (3)            | (4)              | (5)                  | (6)          | (7)                 | (8)          | (9)                 | (10)             | (11)                 |
| S212       | 1.25 | 332            | 0                | 249                  | 13           | 68                  | 4            | 30                  | 123              | 87                   |
| S237       | 0.99 | 305            | 3                | 0                    | 0            | 160                 | 0            | 69                  | 0                | 54                   |
| M42        | 0.44 | 182            | 8                | 263                  | 11           | 92                  | 3            | 14                  | 10               | 118                  |
| S255       | 1.53 | 407            | 10               | 20                   | 5            | 152                 | 1            | 64                  | 4                | 73                   |
| S257       | 0.88 | 208            | 0                | 22                   | 5            | 125                 | 2            | 58                  | 4                | 79                   |
| S271       | 1.29 | 319            | 0                | 8                    | 2            | 140                 | 2            | 48                  | 3                | 29                   |
| S275       | 1.03 | 182            | 5                | 203                  | 11           | 41                  | 2            | 22                  | 8                | 68                   |
| S288       | 1.09 | 291            | 14               | 171                  | 10           | 77                  | 2            | 20                  | 7                | 94                   |
| RCW 6      | 0.79 | 278            | 5                | 186                  | 13           | 94                  | 4            | 50                  | 11               | 189                  |
| RCW 5      | 1.14 | 346            | 137              | 1431                 | 16           | 85                  | 7            | 75                  | 27               | 259                  |
| RCW 8      | 1.83 | 423            | 0                | 7                    | 3            | 144                 | 1            | 53                  | 1                | 86                   |
| S307       | 1.42 | 300            | 0                | 43                   | 6            | 129                 | 1            | 39                  | 4                | 90                   |
| RCW 16     | 0.67 | 180            | 16               | 384                  | 12           | 40                  | 4            | 15                  | 13               | 194                  |
| RCW 34     | 1.91 | 250            | 10               | 122                  | 11           | 103                 | 4            | 31                  | 0                | 185                  |
| RCW 40     | 1.30 | 380            | 0                | 64                   | 10           | 152                 | 5            | 43                  | 11               | 163                  |
| RCW 48     | 1.67 | 241            | 56               | 783                  | 10           | 83                  | 4            | 47                  | 20               | 188                  |
| RCW 53     | 0.87 | 405            | 10               | 210                  | 10           | 102                 | 4            | 32                  | 12               | 126                  |
| NGC 3603   | 2.80 | 172            | 47               | 584                  | 12           | 27                  | 5            | 6                   | 19               | 163                  |
| RCW 62     | 1.02 | 293            | 3                | 147                  | 10           | 60                  | 4            | 13                  | 10               | 118                  |
| M8         | 0.64 | 249            | 4                | 147                  | 11           | 132                 | 3            | 18                  | 12               | 135                  |
| M16        | 0.89 | 212            | 3                | 118                  | 12           | 128                 | 3            | 30                  | 10               | 89                   |
| M17        | 1.24 | 132            | 20               | 437                  | 14           | 53                  | 4            | 13                  | 16               | 121                  |
| S99        | 1.84 | 194            | 6                | 230                  | 14           | 56                  | 4            | 22                  | 11               | 118                  |
| S100       | 1.99 | 101            | 32               | 560                  | 16           | 31                  | 5            | 9                   | 16               | 138                  |
| S148       | 1.28 | 317            | 0                | 10                   | 5            | 187                 | 1            | 60                  | 10               | 189                  |
| S152       | 1.59 | 325            | 0                | 113                  | 11           | 118                 | 3            | 28                  | 11               | 146                  |
| S156       | 1.43 | 297            | 2                | 121                  | 12           | 121                 | 4            | 25                  | 13               | 148                  |
| S158       | 1.70 | 168            | 15               | 403                  | ...          | 38                  | 3            | 16                  | 13               | 120                  |
| S162       | 0.77 | 226            | 2                | 172                  | ...          | 98                  | 2            | 21                  | 9.4              | 160                  |
| N11B       | 0.39 | 310            | 19               | 406                  | 11           | 25                  | 4            | 22                  | 11               | 103                  |
| N44        | 0.22 | 413            | 12               | 297                  | 8            | 36                  | 3            | 44                  | 9                | 110                  |
| N138D,B    | 0.25 | 299            | 69               | 1048                 | 13           | 19                  | 0            | 52                  | 19               | 169                  |
| N51D       | 0.37 | 470            | 8                | 242                  | 12           | 26                  | 3            | 40                  | 7                | 75                   |
| N144       | 0.30 | 293            | 26               | 419                  | 9            | 26                  | 4            | 33                  | 11.              | 113                  |
| N57C       | 0.28 | 226            | 58               | 891                  | 14           | 27                  | 4            | 47                  | 14               | 109                  |
| 30 Dor     | 0.62 | 245            | 40               | 569                  | 11           | 15                  | 4            | 19                  | 11               | 110                  |
| N70        | 0.25 | 478            | 13               | 243                  | 12           | 36                  | 3            | 75                  | 11               | 82                   |
| N180       | 0.38 | 328            | 20               | 373                  | 11           | 25                  | 4            | 28                  | 9                | 86                   |
| N66        | 0.28 | 122            | 49               | 752                  | 9            | 6                   | 3            | 14                  | 9                | 58                   |



This figure "fig2a.jpg" is available in "jpg" format from:

<http://arxiv.org/ps/astro-ph/0002180v1>

This figure "fig2b.jpg" is available in "jpg" format from:

<http://arxiv.org/ps/astro-ph/0002180v1>

This figure "fig2c.jpg" is available in "jpg" format from:

<http://arxiv.org/ps/astro-ph/0002180v1>



This figure "fig2d.jpg" is available in "jpg" format from:

<http://arxiv.org/ps/astro-ph/0002180v1>

This figure "fig2e.jpg" is available in "jpg" format from:

<http://arxiv.org/ps/astro-ph/0002180v1>

This figure "fig2f.jpg" is available in "jpg" format from:

<http://arxiv.org/ps/astro-ph/0002180v1>

This figure "fig2g.jpg" is available in "jpg" format from:

<http://arxiv.org/ps/astro-ph/0002180v1>

